EurJIC
European Journal of Inorganic Chemistry

Research Article
doi.org/10.1002/ejic.202400434

Chemistry Europe
European Chemical Societies Publishing

www.eurjic.org

Metal-Halide–Melem Compounds Based on M_6-, M_9- and M_{12}-Clusters

Markus Ströbele,[a] David Enseling,[b] Thomas Jüstel,[b] Mojtaba Abbasi,[c] Scott Kroeker,[c] and Hans-Jürgen Meyer*[a]

M_9- and M_{12}-metal clusters appear as face-sharing double-clusters in $(Pb_9Br_{19})_2(Pb_{1.5}Br_2)_2(melem)_3$ **(6)** and as triple-clusters in $(Pb_{12}Br_{25})_4(Pb_{1.67}Br_2)_3(melem)_4$ **(7)**. All compounds are characterized by single-crystal and powder X-ray diffraction, and further validated by infrared (IR) spectroscopy and ^{207}Pb and $^{79/81}Br$ NMR studies on **(5)**. Photoluminescence studies on compound **(6)** reveal emission at 430 nm while the emission of **(5)** is completely quenched.

Introduction

The discovery of melamine by Justus von Liebig was fundamental for the development of several fields of chemistry. Today, melamine (2,4,6-triamino-1,3,5-triazine, $C_3N_3(NH_2)_3$) ranks among the top 1,000 substances on the global list of "High production Volume Chemicals," with an annual production of approximately two million tons.[1] Melam is a compound that can be obtained from melamine and was first synthesized in 1834 by heating potassium thiocyanate with ammonium chloride.[2] The conversion of melamine into melem has since been studied by various researchers.[3–6] Melem can be formed through the decomposition and condensation of melamine or its fragments, such as cyanamide and dicyandiamide.[7] Solid-state reactions involving melamine become more complex at elevated temperatures, due to condensation reactions. Specifically, upon heating, melamine transforms into melam ($C_6N_{11}H_9$) at 360 °C[3] (340 °C)[8] and then into melem ($C_6N_{10}H_6$) at about 400 °C[3] (380 °C)[8] under elimination of ammonia.[3,8] Recent studies have successfully completed the crystal structure and spectroscopic characterization of melem.[8–9] During the intermediate stages, the formation of melam or three different melamine-melem adducts is observed.[8,10] Although melam is only stable under certain heating conditions, its identification has contributed to understanding the various mechanisms for melem formation.[3–6]

Similar to other s-triazine (cyanuric nuclei) and s-heptazine (cyameluric nuclei) compounds, melamine, and melem tend to have layered molecular arrangements with intra- and interlayered interactions, such as hydrogen bonding and π-π stacking.[11–14] Due to the high thermal stability of these compounds, melamine resins are used in laminates (e.g. for flooring) or melamine foam as insulation soundproofing building material or for high-resistance concrete. Melamine and its non-metal salts like melamine phosphate[15] or melamine cyanurate[16] are furthermore used as fire-retardant additives, e.g. in paper, plastics, or paints.[17] Similarly, melem and its derivatives are used as flame-retardant materials.[11]

The chemical behavior of melamine has been widely studied to date. Common reactions between metal compounds and melamine were reported in an aqueous solution, leading to melamine compounds in which melamine acts as a base. A well-known example is the melamine-cyanurate compound.[18] Corresponding reactions between melamine and metal salts are reported to yield examples like $[Cu_2(C_3N_6H_6)_2Cl_2]_n$,[19] $[Cu_2(C_3N_6H_6)Br_2]_n$, $[Cu_3Cl_3(C_3N_6H_6)]_n$,[20] $[Cu(C_3H_6N_6)(\mu\text{-}OCH_3)(ONO_2)(HOCH_3)]_2$,[21] $[Ag(C_3H_6N_6)]NO_3$,[22] $(C_3N_6H_7)[HgCl_3](C_3N_6H_6)$,[23] $(C_3H_7N_6)_2[ZnCl_4]\cdot H_2O$,[24] $[Zn(C_3N_6H_6)(H_2O)_{0.5}Cl_2]\cdot(C_3N_6H_6)(H_2O)$,[25] and (cyanuric acid-melamine) CAM–Ag nanofibers[26] from aqueous solutions.

Furthermore, several solid-state reactions between melamine and metal salts have led to novel metal-melaminate compounds, under mild heating conditions. These compounds contain deprotonated melamine which is bonded covalently with the respective metal center. Examples of melaminates involve $(SbCl(C_3N_6H_4))$[27] and $(Cu_3(C_3N_6H_3)$[28] containing twofold and threefold deprotonated melamine, respectively. Solid-state reactions at elevated temperatures can be considerably more complex because pure melamine ($C_3N_6H_6$) undergoes condensation reactions. Within our present studies, we are exploring solid-state reactions between metal salts and melamine at elevated temperatures. This can involve the development of melaminates, or the condensation of melamine rings resulting in the formation of melam or melem and compounds thereof,[8,29] or even the breakdown of the melamine ring with

[a] M. Ströbele, H.-J. Meyer
Section for Solid State and Theoretical Inorganic Chemistry, Institute of Inorganic Chemistry, University of Tübingen, Auf der Morgenstelle 18, D-72076 Tübingen, Germany
E-mail: juergen.meyer@uni-tuebingen.de

[b] D. Enseling, T. Jüstel
University of Applied Sciences, Department Chemical Engineering, Steg-erwaldstrasse 39, D-48565 Steinfurt, Germany

[c] M. Abbasi, S. Kroeker
Department of Chemistry, University of Manitoba, Winnipeg, R3T 2N2, Canada

Supporting information for this article is available on the WWW under https://doi.org/10.1002/ejic.202400434

Research Article
doi.org/10.1002/ejic.202400434

the formation of cyanamide.[30] Correspondingly, the reaction between melamine and indium trichloride has led to the melaminate tetramer, $[C_{12}N_{20}H_8]^{4-}$ in $(NH_4)[(InCl_2)_3(C_{12}N_{20}H_8)]$ at 400 °C.[31] In addition, a limited number of metal-halide–melam compounds have been synthesized by reacting melamine with metal chlorides at elevated temperatures, such as LiBr(melam),[32] LiI(melam),[33] CuBr(melam),[34] and $ZnCl_2$(melam).[8] This underscores the importance of melamine and melem's reactivity at higher temperatures.

Unlike melamine, the chemical reactivity of melem has been investigated in only a few studies. Similar to melamine, one challenge in studying the reactivity of this s-heptazine unit is its insolubility in most organic solvents. The previous studies are more focused on reporting the reactivity of NH_2-groups of melem including tris(trimethylsilylamino)-s-heptazines and tris(tri-n-butylstannylamino)-s-heptazines, trimethylolmelem,[35] trihydrazino-s-heptazine $C_6N_7(NH\text{-}NH_3)_3$, and iminophosphoranes $C_6N_7(N{=}PR_3)_3$.[11] Other studies include the reaction of melem in mineral acids which produces $C_6N_7(NH_2)_3\cdot H_3PO_4$, $H_2C_6N_7(NH_2)_3SO_4\cdot 2H_2O$, $HC_6N_7(NH_2)_3ClO_4\cdot C_6N_7(NH_2)_3$, etc.[36–37] In recent research, Xu et al. identified the only known example of a metal-coordinated compound involving a melem unit, where silver (Ag–N) is bonded to the melem structure.[38] So far, no metal-halide–melem compounds have been studied. In this work, we report on the formation of metal-halide–melem compounds of the binary metal halides $CaBr_2$, $SrBr_2$, SrI_2, BaI_2, and $PbBr_2$ with melem, which we denote as cluster compounds. The term "cluster" was originally used for the description of compounds containing metal atoms connected by metal-to-metal bonds.[39] Today, the term is also used for compounds comprising an ensemble of metal atoms that are interconnected through bridging ligands. Sometimes the term "coordination cluster" is used.[40]

Results and Discussion

Reactions with melamine at elevated temperatures require careful control of the temperature and the duration of the heating process, due to the condensation reaction of melamine itself, the formation of gaseous products, and simultaneous reactions with a given reaction partner. Hence, even the gas pressure in the reaction vessel can have a significant impact on the product formation.[28]

Our initial reactions were carried out using mixtures of melamine and MX_2 salts (M=Ca, X=Br; Sr, Ba; X=I) in fused silica tubes at temperatures around 550 °C. The resulting crystalline pale-yellow powders were identified as melem compounds.

However, the single-crystal structure refinements based on X-ray diffraction data appeared unsatisfactory. This finding prompted us to employ melem in reactions, which is easily prepared from melamine.[41]

Reactions of mixtures of melem and MX_2 salts (M=Ca, Sr, Ba; X=Br, I) were performed in fused silica tubes at temperatures between 430 °C and 550 °C (see Experimental Section). Crystalline powders and single crystals obtained from reactions were selected for subsequent studies.

The crystal structures of $M_6X_{12}(C_3N_6H_6)_4$ (M=Ca, Sr, Ba, Pb; X=Br, I) compounds were solved and refined in the tetragonal space group $P4_2/nmc$ based on single-crystal X-ray diffraction data. We illustrate the structures using lead compounds as examples because they represent all structure types, appearing as Pb_6, Pb_9, and Pb_{12} clusters.

$(Pb_6Br_9)Br_3(melem)_4$ (5)

The structure of **(5)** represents several isotypic members having the sum formula $(M_6X_{12})(melem)_4$ of which M=Ca, X=Br **(1)**; M=Sr, X=Br **(2)**, I **(3)**, or M=Ba, X=I **(4)**. Their crystalline products are obtained as white powders.

The main feature in the crystal structure of $(Pb_6Br_9)Br_3(melem)_4$ is the Pb_6 core of the Pb_6Br_9 cluster (Figure 1), which is tetragonally compressed ($d_{Pb(1)\text{-}Pb(1)}$ = 637.57(5) and $d_{Pb(2)\text{-}Pb(2)}$ = 654.29(3) pm). The remaining interatomic distances $d_{Pb(1)\text{–}Pb(2)}$ are 456.78(3) pm. It is clear that these distances do not represent bonding interactions between lead atoms. All eight cluster faces of the octahedral cluster are μ_3-capped by Br ligands and with Br being situated in the center of the cluster, as shown in Figure 1.

Two melem molecules complete the coordination environment of each lead atom of the octahedral cluster by dative bonding via pairs of nitrogen atoms (Figure 2).

Three additional Br^- ions, represented by the two crystallographically distinct Br(4) and Br(5), are present in the structure of $(M_6Br_9)Br_3(melem)_4$ situated in rather unusual environments, encapsulated by melem molecules in two different ways: Br(4) is situated in a tetrahedral arrangement of melem molecules coordinated by central nitrogen atoms of four melem molecules with Br(4)-N distances of 347.2(3) pm (Figure 3, left). Br(5) is surrounded by eight melem molecules, that are arranged following the motif of a bi-capped trigonal prism with their central nitrogen atoms. As a result, Br(5) is surrounded by six amino groups of melem plus two central nitrogen atoms of melem, shown in Figure 3 at right.

To envision the complete crystal structure, we focus on the arrangement pattern of $[Pb_6Br_9]^{3+}$ cluster units and [Br-

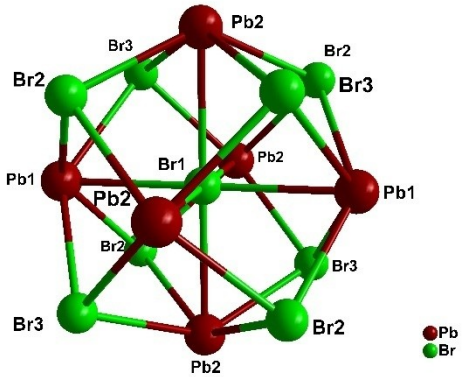

Figure 1. Pb_6Br_9 cluster in **(5)**. Pb atoms are drawn in red, and Br atoms in green.

Research Article
doi.org/10.1002/ejic.202400434

Chemistry Europe
European Chemical Societies Publishing

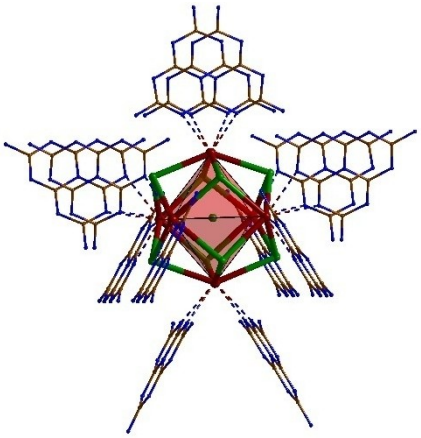

Figure 2. Arrangement of the melem molecules around the Pb_6Br_9 cluster in **(5)**. Pb atoms are drawn in red, Br atoms in green, N atoms in blue, C atoms in brown.

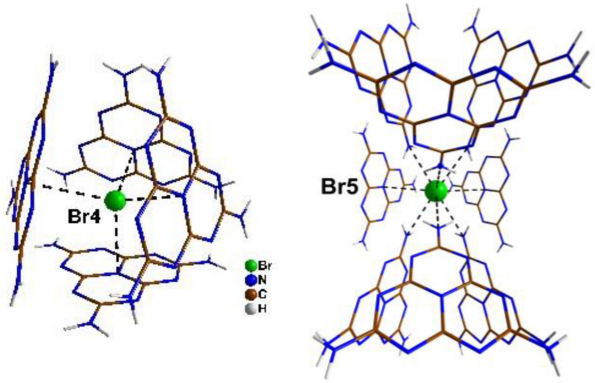

Figure 3. Perspective view of the coordination environment of Br(4) and Br(5) in **(5)**. Br atoms are drawn in green, N atoms in blue, C atoms in brown, and H atoms in white.

$(melem)_4]^-$ units of Br(4), which adopt a CsCl-type structure. In addition, there are two Br^- (Br(5)) situated in the interstices of the CsCl-type arrangement (Figure 4).

$(Pb_9Br_{19})_2(Pb_{1.5}Br_2)_2(melem)_3$ (6)

The compound crystallizes with hexagonal symmetry in the space group $P6_3/mmc$ (No. 194), forming transparent white block-shaped crystals. The structure is represented by face-sharing double-clusters with the Pb_9 core based on two distinct lead atoms. The $[Pb_9Br_{19}]^-$ unit (Figure 5 left) is structurally related to the corresponding cluster units in the structures of $Co_9Se_{11}(PPh_3)_6$[42] and Mo_9E_{11} (E═S, Se)[43] (Figure 5, right). In addition to this pattern, one melem molecule completes the coordination environment of each Pb atom by dative bonding via pairs of nitrogen atoms (Figure 6).

The connectivity of adjacent cluster units in the structure by Br ligands leads to a $[Pb_9Br_{19}]^-$ cluster shown (with cut-through bonds) in Figure 6. The given connectivity leads to a pseudo-hexagonal arrangement in the structure, in which adjacent

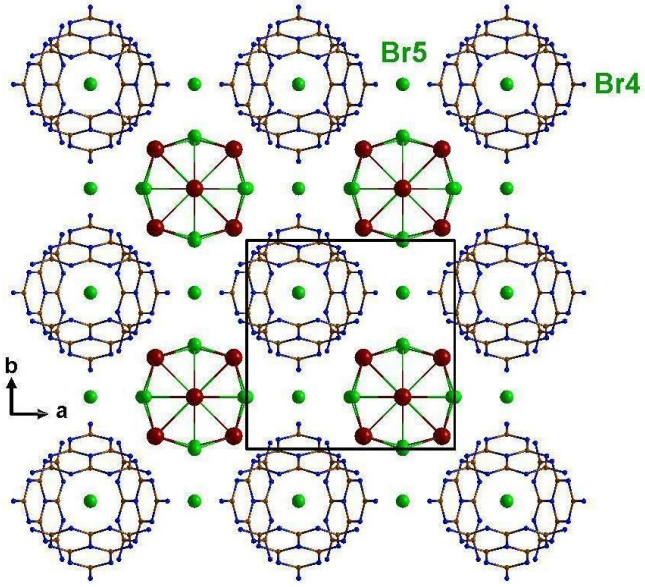

Figure 4. CsCl-type structure arrangement in **(5)**. Pb atoms are drawn in red, Br atoms in green, N atoms in blue, C atoms in brown. The black square marks the unit cell.

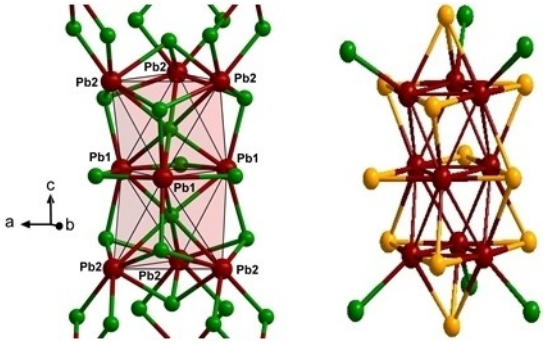

Figure 5. Comparison of the $[Pb_{12}Br_{29}]^-$ cluster unit in **(6)** with the $[Re_9Se_{11}Br_6]^{2-}$ cluster unit in $[PPh_4]_2[Re_9Se_{11}Br_6]$. Pb atoms are drawn in red, Br atoms in green, and Se atoms in orange.

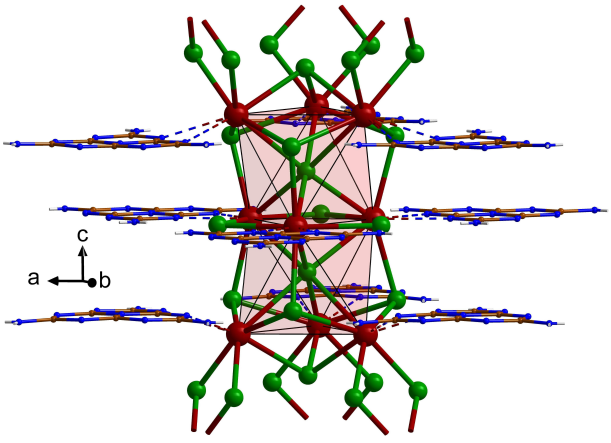

Figure 6. Side-on coordination of melem molecules on Pb atoms in **(6)**. Pb atoms are drawn in red, Br atoms in green, N atoms in blue, C atoms in brown, and H atoms in white.

Research Article
doi.org/10.1002/ejic.202400434

clusters are bridged by two Br ligands (Figure 7, left). The resulting arrangement leaves channels perpendicular to the *ab*-plane (Figure 7 right). Located in these channels are disordered $PbBr_x$ molecules (Figure S1). One additional Br^- is located on a partially occupied 2c position, coordinated by amino groups of three melem molecules (Figure S2).

$(Pb_{12}Br_{25})_4(Pb_{1.67}Br_2)_3(melem)_4$ (7)

The compound crystallizes with monoclinic symmetry in the space group *C*2/*c* (No. 15) appearing with amber-coloured crystal plates. The basic structure element is a triple-cluster with the Pb_{12} core (Figure 8). The presence of four crystallographically distinct Pb_{12} clusters, each of them being based on six distinct lead atoms in the structure, make a complex crystal structure with 24 independent lead atoms (Pb(1)-(6), Pb(7)-(12), Pb(13)-(18), and Pb(19)-(24)).

The arrangement of bromide ligands of the $(Pb_{12}Br_{25})^-$ cluster anion can be expressed as $(Pb_{12}[(\mu_6\text{-}Br)_3(\mu_3\text{-}Br)_{10}(\mu_2\text{-}Br)_6]^{i-i}[\mu_3\text{-}Br_{18/3}]^{i-a})^-$.[44] The coordination environment of the three crystallographically distinct Pb atoms, Pb(4), Pb(5), and Pb(6), is completed by one melem molecule each, by dative bonding via pairs of nitrogen atoms (Figure 8).

Every $(Pb_{12}Br_{25})^-$ cluster unit is interconnected by 12 shared (μ_2-bridging) bromide ligands with six further cluster anions (Figure 9).

Additionally, three crystallographically distinct Pb atoms (Pb(25), Pb(26), Pb(27)) are present in channels of the structure (Figures S3, S4). The crystallographic positions of Pb(26) and Pb(27) are 75% occupied. The resulting composition can be given as $(Pb_{12}Br_{25})_4(Pb_{1.67}Br_2)_3$ and the unit cell is depicted in Figure 10 with the $(Pb_{12}Br_{25})^-$ ions forming tilted corrugated layers with the additional Pb atoms located in the channels and melem molecules stacked along the [100] direction.

Infrared Spectroscopy

The infrared (IR) spectra recorded for **(1)** to **(7)** are presented in Figure 11 in comparison to that of melem.[45] Table S1 lists the

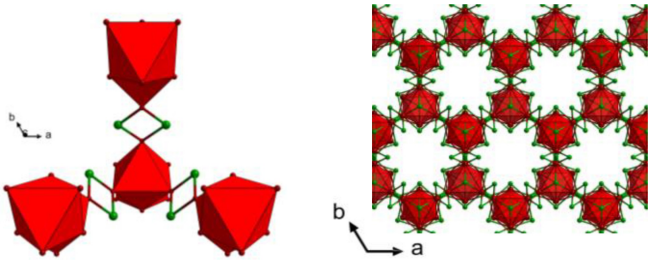

Figure 7. Perspective drawing of the interconnection between $(Pb_9Br_{19})^-$ cluster anions by μ_2-bridging Br atoms in **(6)** at left (terminal Br atoms are suppressed for more clarity) and a projection of the structure of **(6)** emphasizing channels perpendicular to the *ab*-plane. Pb atoms are drawn in red, and Br atoms in green.

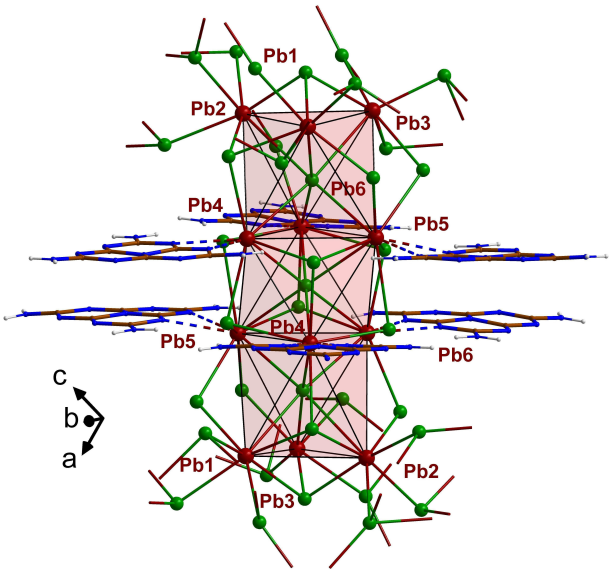

Figure 8. Section of the $[Pb_{12}Br_{29}]^-$ cluster carrying four melem molecules in the structure of **(7)**. Pb atoms are drawn in red, Br atoms in green, N atoms in blue, C atoms in brown, and H atoms in white.

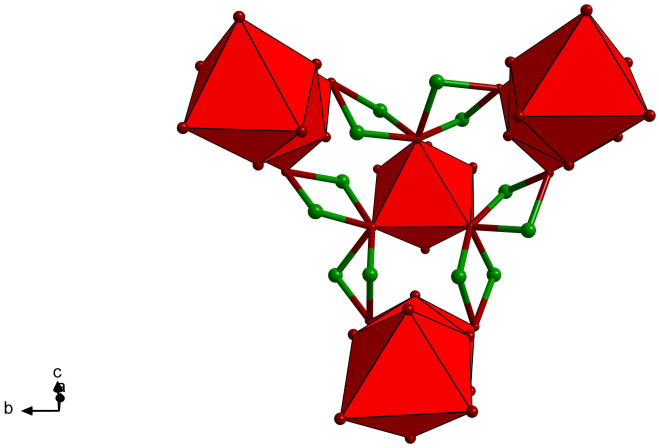

Figure 9. Perspective drawing of the interconnection between $(Pb_{12}Br_{25})_2^-$ cluster anions by μ_2-bridging Br atoms in **(7)**. Pb atoms are drawn in red, and Br atoms in green. Non-bridging Br atoms are omitted for clarity.

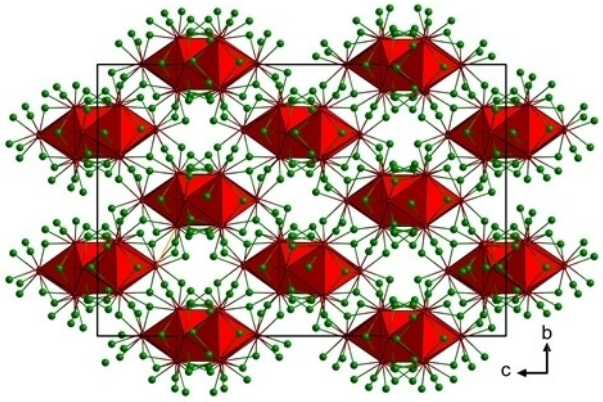

Figure 10. Projection of the unit cell content $(Pb_{12}Br_{25})_4(Pb_{1.67}Br_2)_3$ of **(7)**. Pb_{12} clusters are highlighted as red polyhedra, Pb atoms are drawn in red, and Br atoms in green.

Research Article
doi.org/10.1002/ejic.202400434

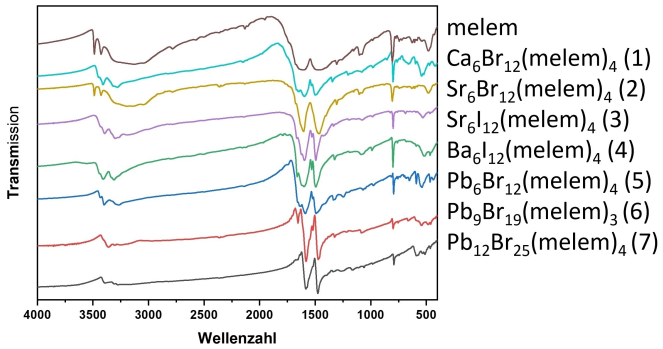

Figure 11. Comparison of the IR spectra of (**1**) to (**7**) with the IR spectrum of melem.

wavenumbers along with each vibrational mode of these molecules, along with the corresponding bond assignments. IR absorption bands indicative of the asymmetric and symmetric stretching of -NH_2 groups of melem can be found in the range 3500–3200 cm^{-1} of the melem spectrum and due to coupling the peaks are broadened.[46–47] The bending mode of the NH_2 groups in these compounds is in the range of 1580–1606 cm^{-1}.

The two strongest IR bands of the compounds in the region 1502–1465 cm^{-1} are assigned to side chain C–N breathing, in the region around 1335 cm^{-1} to C–N–C bending modes. The bands in the region 804–793 cm^{-1} are assigned to ring-sextant out-of-plane bending modes.

NMR Spectroscopy on $(Pb_6Br_9)Br_3(melem)_4$ (5)

The ^{207}Pb NMR spectrum of powdered (**5**) yields a pattern that reflects moderately anisotropic magnetic shielding, spanning a breath of 600 ± 10 ppm (Figure 12). Compared to other coordination polymers involving nitrogenous donors with documented shielding spans ranging from 400 to 4000 ppm,[48–50] this value is relatively small. The anisotropic character of ^{207}Pb magnetic shielding is very sensitive to the Pb^{2+} local electronic environment and provides a measure of the stereochemical activity of the lone pair, with holodirectional bonding corresponding to smaller spans, and hemidirectional bonding giving rise to large shielding spans.[49] The establishment of more precise structural metrics is complicated by the wide variety of bonding environments found for closely related coordination polymers. For example, a series of seven Pb[2,6-bis(benzimidazol-2-yl)pyridine] complexes with coordination numbers ranging from 7 to 9 have varying degrees of distortion from idealized polyhedral geometry giving rise to measured δ_{iso} values ranging from +30 to −2950 ppm, and Ω values differing by over 1000 ppm.[48] Attempts to rationalize these variations in terms of more quantitative structural parameters have met with some degree of success for closely related compounds, with reasonable correlations found between Ω and the shortest Pb–N bond length, the axial angle between trans-N ligands,[48] and the Pb–N bond-length distortion parameter.[49]

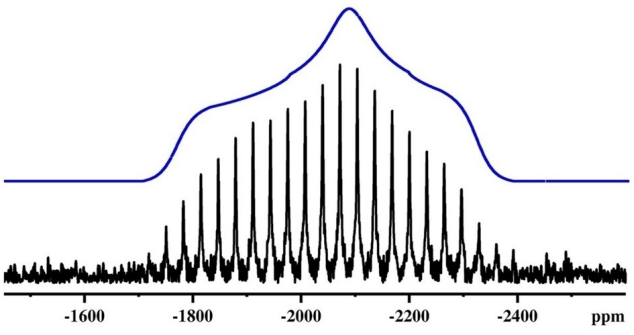

Figure 12. ^{207}Pb WURST CPMG NMR of (**5**) with a fit based on anisotropic shielding parameters (see text).

The bonding environments of Pb(1) and Pb(2) in (**5**) are very similar and both contain four bonds to melem N atoms and four contacts to Br in the Pb_6 cluster, producing a nominally holodirectional coordination sphere, however with all N occupying one hemisphere and all Br in the other. The high degree of structural similarity of these two crystallographically inequivalent sites makes them indistinguishable in the low-resolution ^{207}Pb spectrum obtained. However, it is clear that the magnetic shielding arising from this arrangement is remarkably isotropic, implying that the electronic environment of Pb^{2+} is quite symmetrical, despite the different bonding partners in each hemisphere. This may be compared with $[Pb(bbp)Br_2][Hg(CN)_2]$, in which the Pb bonds to three nitrogen ligands in the tridentate bbp ligand, and three bromide ligands, each occupying separate hemispheres, resulting in ^{207}Pb shielding parameters ($\delta_{iso} = -2600$ ppm, $\Omega = 700$ ppm) that are quite similar to those of (**5**) and much closer than any of the other compounds in that series.[48]

In contrast to ^{207}Pb NMR, where the anisotropic shielding provides a sensitive measure of local structure, the $^{79/81}$Br NMR signals are dominated by the interaction of their large nuclear quadrupole moments with the local electric field gradient.[51] This is quantified by the quadrupole coupling constant, C_Q, which varies from zero to more than 600 MHz[52] for ^{81}Br in some compounds, only a small fraction of this range being observable by NMR spectroscopy. The spectroscopic challenge of compound (**5**) arises both from the highly asymmetric environments of two of the Br sites, as well as the very different degrees of symmetry around the five Br, thereby preventing the observation of all five in a single spectrum obtained by a single NMR method. However, with knowledge of the Br coordination environments from the crystal structure, reasonable assignments of the signals found in Br NMR experiments may be made.

The ^{81}Br magic-angle spinning (MAS) NMR spectrum of (**5**) collected under routine Bloch-decay conditions yielded only a single sharp peak (Figure S12), with evidence of low-intensity, unresolved signals extending out 600 ppm in either direction. Considering the large magnitude of the nuclear electric quadrupole moment of ^{81}Br, only a highly symmetrical site could produce a small enough electric field gradient to result in such a narrow peak. Of the five Br environments in (**5**), only Br(1), at the center of the Pb_6Br_9 cluster, satisfies this requirement. Turning to ^{79}Br, with a slightly smaller quadrupole moment, the

Research Article
doi.org/10.1002/ejic.202400434

WURST QCPMG spectrum of a non-spinning sample reveals distinct features characteristic of second-order quadrupolar effects (Figure S13). (It may be noted that this pulse sequence cannot observe narrow signals, such as that of Br(1).) The singularities may be satisfactorily fit as two axially-symmetric, central-transition line shapes with C_Q values of 12.8(1) and 13.5(1) MHz in equal abundance. The chemical shift values of 460(10) and −280(10) ppm, respectively, are well separated, but less structurally informative than the quadrupolar parameters. In particular, the rigorous axial symmetry ($\eta = 0$) of these sites suggests that they are located on rotation axes, which is consistent with the crystallographic data as Br(4) is located on a 2b position (−4 m2) and Br(5) on a 4d position (2 mm), and the relatively small C_Qs indicate that they are in fairly symmetric environments, such as the tetrahedral arrangements of melem molecules shown in Figure 3. Finally, the highly asymmetrical bonding environments of Br(2) and Br(3) in the Pb_6Br_9 cluster are expected to have extremely large C_Q values. Although they are probably not amenable to precise measurement by NMR, an expanded view of the WURST QCPMG spectrum shows significant, if indistinct, intensity between 2000–4000 ppm and −2000 to −5000 ppm (Figure S13). This signal cannot be accounted for as satellite transitions of Br(4) and Br(5), but very likely arises from Br(2) and/or Br(3). While this cannot be confirmed without resorting to ultrahigh-field NMR or even nuclear quadrupole resonance,[52] it does help to explain slight discrepancies in the fitted signal intensities shown in Figure 13. In summary, the $^{79/81}$Br NMR responses of **(5)** are consistent with its structural features, and highlight the remarkable sensitivity of this nucleus as a probe of different local structural environments.

Luminescence of (6)

The excitation spectrum of compound **(6)** monitored for the maximum of the emission band at 481 nm is depicted in Figure 14. At 100 K it shows an intense broad band at 385 nm (26000 cm^{-1}), which is extinguished at 250 K. Moreover, a weak band at 335 nm (29900 cm^{-1}) appears, which is already totally quenched at 150 K.

Figure 14 also comprises the emission spectrum of compound **(6)** under 386 nm excitation and shows a broad emission band peaking at 481 nm (21700 cm^{-1}) with a full width at half maximum of 35 nm (1500 cm^{-1}). Therefore, the Stokes shift of the emission band is about 4300 cm^{-1}, which is rather small for the photoluminescence of $6s^2$ ions (Tl^+, Pb^{2+}, Bi^{3+}). The intensity of the photoluminescence is strongly temperature-dependent and almost completely quenched at room temperature.

The observed strong photoluminescence is assigned to an interconfigurational $[Xe]4f^{14}5d^{10}6s^2$ ($^1S_0$) to $[Xe]4f^{14}5d^{10}6s^16p^1$ ($^1P_1$, ^3P_J with $J = 0,1,2$) transition of Pb^{2+}. The detailed interpretation of the s^2 luminescence was done by Seitz for Tl^+ activated phosphors a long time ago, while most of the Tl^+ and Pb^{2+} show a single emission band located in the UV range.[53–54] The ground state of the $6s^2$ configuration is $^1S_0$, while the excited configuration comprises four electronic states due to

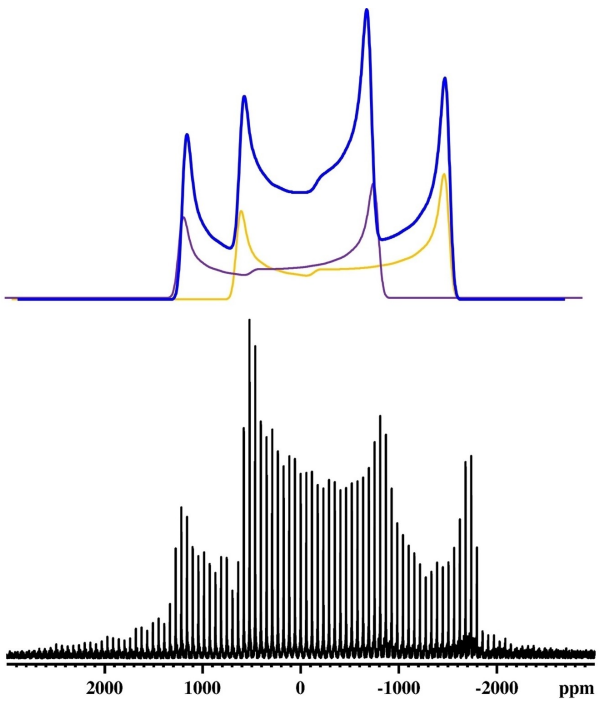

Figure 13. ^{79}Br WURST QCPMG NMR of **5**, showing the central transitions of two of the five Br sites. Simulated subspectral contributions of Br(4) and Br(5) are shown in purple and yellow, while the overall spectral fit from these two sites is shown in blue. (See Figure S13 for a wider spectral view, and Figure S12 for the MAS spectrum.)

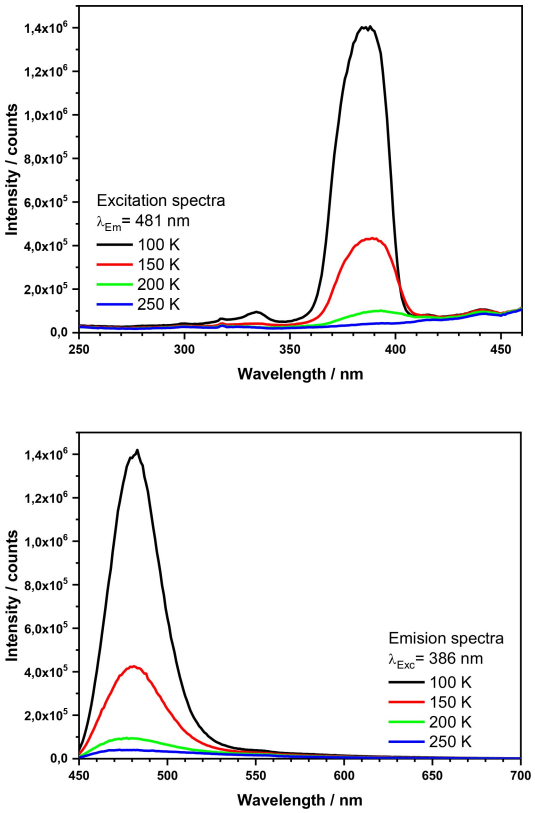

Figure 14. Excitation (top) and emission (bottom) spectra of **(6)** between 100 and 250 K in 50 K steps.

Research Article
doi.org/10.1002/ejic.202400434

the large spin-orbit coupling of the $^3P_{0,1,2}$ state.[55–56] The observed bands in the excitation spectrum are assigned to the $^1S_0 \rightarrow {}^3P_2$ (335 nm) and $^1S_0 \rightarrow {}^3P_1$ (385 nm) transitions.

Remarkable is the low energy of these two excitation bands and the luminescence band due to the $^3P_0 \rightarrow {}^1S_0$ transition in the cyan-blue range. This might be caused by the interaction of the Pb^{2+} cluster with the electron-rich melem. The transfer of electron density will reduce the effective charge of Pb^{2+} and thus the interconfigurational splitting between the $6s^2$ and $6s^16p^1$ configurations, which will in turn yield red-shifted Pb^{2+} photoluminescence.

Conclusions

The number of metal salt compounds with melamine, melam, or melem (or their protonated or deprotonated forms) is meagre, even if their potential for biological activity,[24] photocatalytic properties,[19] and radiation attenuation[57] is known. These compounds have also potential to help with dynamic leaching of Pb perovskite solar cells[58] as the Pb compounds are stable in air and water. Further investigations of these easy-to-make compounds should be undertaken to explore their properties.

The series of lead-bromide-melem compounds ranging from $(Pb_{12}Br_{25})_4(Pb_{1.67}Br_2)_3(melem)_4$ to $(Pb_9Br_{19})_2(Pb_{1.5}Br_2)_2(melem)_3$ to $(Pb_6Br_9)Br_3(melem)_4$ can be understood as a result of a successively increased concentration of melem in a solution of lead bromide.

Experimental Section

General

All reactions were carried out by mixing and grounding the starting material in an agate mortar under a dry argon atmosphere in a glove box with moisture and oxygen levels below 1 ppm. The reaction mixtures were transferred into homemade silica ampoules (inner diameter 7 mm, l = 7 cm, V ~ 2.5 cm^3) and sealed under vacuum. The reactions were carried out in Simon-Müller furnaces.

Melem ($C_6H_6N_{10}$)

The compound was synthesized as described in the literature.[41]

$(Ca_6Br_9)Br_3(melem)_4$

A mixture of ground starting materials of $CaBr_2$ (333 mg, 0.165 mmol, Sigma-Aldrich, 99.98% trace metals basis) and melem (24.3 mg, 0.111 mmol) was heated to 540 °C at 1 K/min, kept there for 120 h and cooled to room temperature at 0.5 K/min. $(Ca_6Br_9)Br_3(melem)_4$ was obtained as a light yellow, moisture sensitive, phase pure powder, with the refined Rietveld pattern given in Figure S5.

$(Sr_6Br_9)Br_3(melem)_4$

A mixture of ground starting materials of $SrBr_2$ (68 mg, 0.28 mmol, Sigma-Aldrich, 99.99% trace metals basis) and melem (40 mg, 0.18 mmol) was heated to 575 °C at 2 K/min, kept there for 72 h and cooled to room temperature at 0.2 K/min. $(Sr_6Br_9)Br_3(melem)_4$ was obtained as a light yellow, moisture sensitive, with the refined Rietveld pattern given in Figure S6.

$(Sr_6I_9)I_3(melem)_4$

A mixture of ground starting materials of SrI_2 (33.3 mg, 0.098 mmol, Sigma-Aldrich, 99.99% trace metals basis) and melem (14.2 mg, 0.065 mmol) was heated to 550 °C at 1 K/min, kept there for 120 h and cooled to room temperature at 0.5 K/min. $(Sr_6I_9)I_3(melem)_4$ was obtained as a dark yellow, moisture sensitive, phase pure powder, with the refined Rietveld pattern given in Figure S7.

$(Ba_6I_9)I_3(melem)_4$

A mixture of ground starting materials of BaI_2 (33.3 mg, 0.085 mmol, Sigma-Aldrich, 99.995% trace metals basis) and melem (12.4 mg, 0.057 mmol) was heated to 550 °C at 1 K/min, kept there for 120 h and cooled to room temperature at 0.5 K/min. $(Ba_6I_9)I_3(melem)_4$ was obtained as a dark yellow, moisture sensitive, phase pure powder, with the refined Rietveld pattern given in Figure S8.

$(Pb_6Br_9)(melem)_4Br_3$

A mixture of ground starting materials of $PbBr_2$ (33.3 mg, 0.091 mmol, Sigma-Aldrich, 99.999% trace metals basis) and melem (13.2 mg, 0.057 mmol) was heated to 430 °C at 2 K/min, kept there for 48 h and cooled to room temperature at 0.5 K/min. $(Pb_6Br_9)Br_3(melem)_4$ was obtained as a pale yellow powder and transparent white single crystals, used for single crystal determination. The refined Rietveld pattern is given in Figure S9.

$(Pb_9Br_{19})_2(Pb_{1.5}Br_2)_2(melem)_3$

A mixture of ground starting materials of $PbBr_2$ (66.67 mg, 0.18 mmol, Sigma-Aldrich, 99.999% trace metals basis) and Melem (11.9 mg, 0.055 mmol) was heated to 475 °C at 2 K/min, kept there for 48 h and cooled to room temperature at 0.5 K/min. $(Pb_9Br_{19})_2(Pb_{1.5}Br_2)_2(melem)_3$ was obtained as a pale yellow, phase-pure powder and white transparent block-like crystals used for single crystal determination. The refined Rietveld pattern is given in Figure S10.

$(Pb_{12}Br_{25})_4(Pb_{1.67}Br_2)_3(melem)_4$

Starting material $PbBr_2$ (100 mg, 0.27 mmol, Sigma-Aldrich, 99.999% trace metals basis) and Melem (8.8 mg, 0.04 mmol). The mixture was heated to 500 °C at 2 K/min, kept there for 24 h, and cooled to room temperature at 0.2 K/min. $(Pb_{12}Br_{25})_4 \cdot (Pb_{1.67}Br_2)_3(melem)_4$ was obtained as a pale yellow, phase pure powder and yellow thin plate-like single crystals, used for structure determination. The refined Rietveld pattern is given in Figure S11.

CCDC 2127410 contains the supplementary crystallographic data for $Ca_6Br_{12}(C_6H_6N_{10})_4$, CCDC 2312729 for $Sr_6Br_{12}(C_6H_6N_{10})_4$, CCDC 2127277 for $Sr_6I_{12}(C_6H_6N_{10})_4$, CCDC 2127294 for $Ba_6I_{12}(C_6H_6N_{10})_4$, CCDC 2143207 for $Pb_6Br_{12}(C_6H_6N_{10})_4$, CCDC 2165848 for

Research Article
doi.org/10.1002/ejic.202400434

$Pb_{10}Br_{20}(C_6H_6N_{10})_3$. CCDC 2367566 for $((Pb_{12}Br_{25})_4(Pb_{1.67}Br_2)_3(C_6H_6N_{10})_4$. These data can be obtained free of charge from The Cambridge Crystallographic Data Centre via www.ccdc.cam.ac.uk/structures.

Powder X-Ray Diffraction

Compounds were investigated by powder X-ray diffraction (XRD) on a Stadi-P (STOE, Darmstadt) diffractometer with germanium monochromated Cu-$K_{\alpha1}$ radiation. The powder XRD patterns of $Sr_6I_{12}(melem)_4$ were indexed in the space group $P\,4_2/nmc$ (No. 137) and the structure was solved with the program EXPO by direct methods. The structure refinement was carried out with Winplotr (Fullprof), with the final full refinement plot displayed in the Supporting Information.

Single Crystal X-Ray Diffraction

Single clear colourless block-shaped crystals of $(Pb_6Br_9)Br_3(melem)_4$, $(Pb_9Br_{19})_2(Pb_{1.5}Br_2)_2(melem)_3$, and $(Pb_{12}Br_{25})_4(Pb_{1.67}Br_2)_3(melem)_4$ were used as supplied. Suitable single crystals with dimensions 0.09×0.08×0.06 mm^3 ($(Pb_6Br_9)Br_3(melem)_4$), 0.07×0.04×0.03 mm^3 ($(Pb_9Br_{19})_2(Pb_{1.5}Br_2)_2(melem)_3$), and 0.1 x 0.07 x 0.008 mm^3 ($(Pb_{12}Br_{25})_4(Pb_{1.67}Br_2)_3(melem)_4$) were selected and mounted on a XtaLAB Synergy, Dualflex, HyPix diffractometer. The crystals were kept at a steady T = 150.0(1) K during data collection. The structures were solved with the ShelXT 2018/2 (Sheldrick, 2018) solution program using dual methods and by using Olex2 1.3-ac4[59] as the graphical interface. The models were refined with ShelXL 2018/3[60] using full matrix least squares minimisation on F^2.

Infrared Spectra

Infrared (IR) spectra of samples were recorded with a Bruker VERTEX 70 FT-IR spectrometer within the spectral range of 400–4000 cm^{-1}. Tablets of KBr were used as a background.

Luminescence Spectra

Excitation and emission spectra and decay curves were recorded with a fluorescence spectrometer FLS920 (Edinburgh Instruments) equipped with a 450 W xenon discharge lamp (OSRAM). The spectrometer is equipped with a mirror optic for powder samples inside the sample chamber. For the collection of Data, an R2658P single-photon-counting Photomultiplier tube from Hamamatsu was used. For temperature adjustment, a cryostat "MicrostatN" from the Oxford Instruments had been applied to the present spectrometer. Liquid nitrogen was used as a cooling agent. A 375 nm ps Laser from Edinburgh Instruments was used as an excitation source for the decay curves.

NMR Spectra

NMR spectra were acquired at the University of Manitoba on a wide-bore Bruker Avance III spectrometer (B_0 = 9.4 T) using a 4-mm magic-angle spinning (MAS) probe head. The ^{207}Pb wideband uniform-rate, smooth truncation (WURST) Carr-Purcell-Meiboom-Gill (CPMG)[61] spectrum was recorded at 83.50 MHz on a non-spinning sample of 5, with a $\pi/2$ pulse width of 3.275 μs at 76.3 kHz. 1200 transients were collected with a recycle delay of 50 s. The spectrum is referenced to a 1 M solution of $Pb(NO_3)_2$ at −2961 ppm.[62] ^{79}Br WURST quadrupolar CPMG (QCPMG) spectra were acquired at 100.21 MHz with a $\pi/2$ pulse width of 2.8 μs at 89.2 kHz, 8000 transients, and a recycle delay of 1 s. For both ^{207}Pb and ^{79}Br, 50-μs WURST-80 pulses were linearly swept from low- to high-frequency, covering a total range of 1 MHz. The ^{79}Br NMR spectrum was acquired piece-wise by moving the transmitter and coadding three separate spectra post-acquisition. A ^{81}Br MAS NMR spectrum of (5) was collected on a Varian Unity Inova 600 MHz spectrometer using a 1.6 mm rotor spinning at 25 kHz, with 1024 scans, a recycle delay of 1 s, and a 30° tip angle. ^{79}Br and ^{81}Br spectra were referenced to solid KBr (0 ppm). Line shape fitting was done with WSOLIDS1.[63] For ^{207}Pb, the isotropic chemical shift (δ_{iso}) obtained from MAS was fixed in the simulation of the non-spinning spectrum, and the span (Ω) and skew (κ) were manually adjusted to obtain the best fit.

Acknowledgements

SK is grateful to the Natural Sciences and Engineering Research Council (NSERC) of Canada for support of this work, as well as the Canada Foundation for Innovation (CFI) for infrastructure support. Open Access funding enabled and organized by Projekt DEAL.

Conflict of Interests

The authors declare no conflict of interest.

Data Availability Statement

The data that support the findings of this study are available in the supplementary material of this article.

Keywords: Melamine · Melem · Solid-state reaction · Crystal structures · ^{207}Pb NMR · $^{79/81}Br$ NMR

[1] OECD, The 2004 OECD List of High Production Volume Chemicals,Organisation for Economic Co-operation and Development, Paris, **2004**, p. 21.
[2] L. Gmelin, *Annalen der Pharmacie* **1835**, *15*, 252–258.
[3] H. May, *J. Appl. Chem.* **1959**, *9*, 340–344.
[4] B. Jürgens, E. Irran, J. Senker, P. Kroll, H. Müller, W. Schnick, *J. Am. Chem. Soc.* **2003**, *125*, 10288–10300.
[5] Y. Yi, J. Wang, Y. Niu, Y. Yu, S. Wu, K. Ding, *RSC Adv.* **2022**, *12*, 24311–24318.
[6] B. V. Lotsch, PhD thesis, Ludwig Maximilian University of Munich (Germany) **2006**.
[7] B. V. Lotsch, M. Döblinger, J. Sehnert, L. Seyfarth, J. Senker, O. Oeckler, W. Schnick, *Chem. A Eur. J.* **2007**, *13*, 4969–4980.
[8] B. V. Lotsch, W. Schnick, *Chem. A Eur. J.* **2007**, *13*, 4956–4968.
[9] N. E. Braml, A. Sattler, W. Schnick, *Chem. A Eur. J.* **2012**, *18*, 1811–1819.
[10] A. Sattler, S. Pagano, M. Zeuner, A. Zurawski, D. Gunzelmann, J. Senker, K. Müller-Buschbaum, W. Schnick, *Chem. A Eur. J.* **2009**, *15*, 13161–13170.
[11] A. Schwarzer, T. Saplinova, E. Kroke, *Coord. Chem. Rev.* **2013**, *257*, 2032–2062.
[12] E. Kroke, M. Schwarz, *Coord. Chem. Rev.* **2004**, *248*, 493–532.
[13] M. A. Rossman, N. J. Leonard, S. Urano, P. R. LeBreton, *J. Am. Chem. Soc.* **1985**, *107*, 3884–3890.
[14] A. M. Halpern, M. A. Rossman, R. S. Hosmane, N. J. Leonard, *J. Phys. Chem.* **1984**, *88*, 4324–4326.
[15] A. Castiñeiras, I. García-Santos, J. M. González-Pérez, A. Bauzá, J. K. Zaręba, J. Niclós-Gutiérrez, R. Torres, E. Vílchez, A. Frontera, *Cryst. Growth Des.* **2018**, *18*, 6786–6800.
[16] G. Pieter, S. Rieky, F. Christian, K. Joyce, *Polym. Degrad. Stab.* **2002**, *78*, 219–224.

[17] R. D. Ashford, *Ashford's Dictionary of Industrial Chemicals*, 3rd ed., Wavelength Saltash, London, UK, **2011**.
[18] T. J. Prior, J. A. Armstrong, D. M. Benoit, K. L. Marshall, *CrystEngComm* **2013**, *15*, 5838–5843.
[19] L. Liu, Y. Wu, L. Ma, G. Fan, W. Gao, W. Wang, X. Ma, *J. Struct. Chem.* **2022**, *63*, 302–309.
[20] L. Zhang, J. Zhang, Z.-J. Li, J.-K. Cheng, P.-X. Yin, Y.-G. Yao, *Inorg. Chem.* **2007**, *46*, 5838–5840.
[21] D. M. L. Goodgame, I. Hussain, A. J. P. White, D. J. Williams, *J. Chem. Soc., Dalton Trans.* **1999**, *17*, 2899–2900.
[22] K. Sivashankar, A. Ranganathan, V. R. Pedireddi, C. N. R. Rao, *J. Mol. Struct.* **2001**, *559*, 41–48.
[23] P. Nockemann, G. Meyer, *Z. Anorg. Allg. Chem.* **2004**, *630*, 2571–2572.
[24] T. Salah, N. Mhadhbi, A. Ben Ahmed, B. Hamdi, N. Krayem, M. Loukil, A. Guesmi, L. Khezami, A. Houas, N. Ben Hamadi, H. Naïli, F. Costantino, *Crystals* **2023**, *13*, 746.
[25] Y.-Q. Yu, C.-Z. Lu, X. He, S.-M. Chen, Q.-Z. Zhang, L.-J. Chen, W.-B. Yang, *J. Chem. Crystallogr.* **2004**, *34*, 905–909.
[26] P. Meng, A. Brock, Y. Xu, C. Han, S. Chen, C. Yan, J. McMurtrie, J. Xu, *J. Am. Chem. Soc.* **2019**, *142*, 479–486.
[27] E. Bayat, M. Ströbele, H.-J. Meyer, *Chemistry* **2023**, *5*, 1465–1476.
[28] P. Kallenbach, E. Bayat, M. Ströbele, C. P. Romao, H.-J. Meyer, *Inorg. Chem.* **2021**, *60*, 16303–16307.
[29] F. K. Kessler, A. M. Burow, G. Savasci, T. Rosenthal, P. Schultz, E. Wirnhier, O. Oeckler, C. Ochsenfeld, W. Schnick, *Chem. A Eur. J.* **2019**, *25*, 8415–8424.
[30] M. Becker, M. Jansen, A. Lieb, W. Milius, W. Schnick, *Z. Anorg. Allg. Chem.* **1998**, *624*, 113–118.
[31] E. Bayat, M. Ströbele, D. Enseling, T. Jüstel, H. J. Meyer, *Dalton Trans.* **2024**, *53*, 10912-10918.
[32] M. Ströbele, H.-J. Meyer, *CCDC 2039843: Experimental Crystal Structure Determination* **2020**..
[33] M. Löber, M. Ströbele, H.-J. Meyer, *CCDC 1958336: Experimental Crystal Structure Determination* **2019**.
[34] P. Kallenbach, M. Ströbele, H.-J. Meyer, CCDC 2059117: Experimental Crystal Structure Determination **2022**.
[35] R. Spasskaya, A. Finkel'shtein, E. Zil'berman, V. Gal'perin, *Zh. Obshch. Khim.* **1976**, *46*, 1423.
[36] F. K. Keßler, PhD thesis, Ludwig Maximilian University of Munich **2019**.
[37] A. Sattler, W. Schnick, *Z. Anorg. Allg. Chem.* **2008**, *634*, 457–460.
[38] H. Meng, P. Meng, Z. Liu, J. McMurtrie, J. Xu, *Inorg. Chem.* **2024**, *63*, 6980–6987.
[39] F. Cotton, N. Curtis, C. Harris, B. Johnson, S. Lippard, J. Mague, W. Robinson, J. Wood, *Science* **1964**, *145*, 1305–1307.
[40] A. T. Wagner, P. W. Roesky, *Eur. J. Inorg. Chem.* **2016**, *2016*, 782–791.
[41] S. Chu, C. Wang, J. Feng, Y. Wang, Z. Zou, *Int. J. Hydrog. Energy* **2014**, *39*, 13519–13526.
[42] D. Fenske, J. Ohmer, J. Hachgenei, *Angew. Chem. Int. Ed. English* **1985**, *24*, 993–995.
[43] A. Gruttner, K. Yvon, R. Chevrel, M. Potel, M. Sergent, B. Seeber, *Acta Crystallogr. Section B* **1979**, *35*, 285–292.
[44] H. Schäfer, H. G. Schnering, *Angew. Chem.* **1964**, *76*, 833–868.
[45] X. Yuan, K. Luo, N. Liu, X. Ji, C. Liu, J. He, G. Tian, Y. Zhao, D. Yu, *Phys. Chem. Chem. Phys.* **2018**, *20*, 20779–20784.
[46] M. Hesse, H. Meier, B. Zeeh, *Spektroskopische Methoden in der organischen Chemie*, Georg Thieme Verlag, **2005**.
[47] P. Larkin, *Infrared and Raman Spectroscopy: Principles and Spectral Interpretation*, 2nd ed., Elsevier, Stamford, CT, United States, **2017**.
[48] J. R. Thompson, D. Snider, J. E. C. Wren, S. Kroeker, V. E. Williams, D. B. Leznoff, *Eur. J. Inorg. Chem.* **2017**, *2017*, 88–98.
[49] B. J. Greer, V. K. Michaelis, M. J. Katz, D. B. Leznoff, G. Schreckenbach, S. Kroeker, *Chem. A Eur. J.* **2011**, *17*, 3609–3618.
[50] M. J. Katz, V. K. Michaelis, P. M. Aguiar, R. Yson, H. Lu, H. Kaluarachchi, R. J. Batchelor, G. Schreckenbach, S. Kroeker, H. H. Patterson, D. B. Leznoff, *Inorg. Chem.* **2008**, *47*, 6353–6363.
[51] P. M. J. Szell, D. L. Bryce, in *Annual Reports on NMR Spectroscopy*, Vol. 84 (Ed.: G. A. Webb), Academic Press,, London, UK, **2015**, 115–162.
[52] P. Cerreia Vioglio, P. M. J. Szell, M. R. Chierotti, R. Gobetto, D. L. Bryce, *Chem. Sci.* **2018**, *9*, 4555–4561.
[53] F. Seitz, *J. Chem. Phys.* **1938**, *6*, 150–162.
[54] R. H. Clapp, R. J. Ginther, *JOSA* **1947**, *37*, 355–362.
[55] B. C. G. G. Blasse, *Luminescent Materials*, 1. Ed., Springer-Verlag, Berlin, **1994**.
[56] J. L. Musfeldt, *J. Am. Chem. Soc.* **1999**, *121*, 4310–4310.
[57] O. G. Torres, G. Gordillo, M. C. Plazas, D. A. Landínez Téllez, J. Roa-Rojas, *J. Mater. Sci. – Mater. Electron.* **2021**, *32*, 16937–16944.
[58] P. Su, Y. Liu, J. Zhang, C. Chen, B. Yang, C. Zhang, X. Zhao, *J. Phys. Chem. Lett.* **2020**, *11*, 2812–2817.
[59] O. V. Dolomanov, L. J. Bourhis, R. J. Gildea, J. A. K. Howard, H. Puschmann, *J Appl. Crystallogr.* **2009**, *42*, 339–341.
[60] G. Sheldrick, *Acta Crystallogr. Section C* **2015**, *71*, 3–8.
[61] E. Kupce, R. Freeman, *J. Magn. Reson., Ser. A* **1995**, *115*, 273–276.
[62] G. Neue, C. Dybowski, M. L. Smith, M. A. Hepp, D. L. Perry, *Solid State Nucl. Magn. Reson.* **1996**, *6*, 241–250.
[63] K. Eichele, *WSOLIDS1: Solid-State NMR Simulation*, University of Tuebingen (Germany), **2021**.

Manuscript received: July 9, 2024
Revised manuscript received: September 30, 2024
Accepted manuscript online: September 30, 2024
Version of record online: November 7, 2024